Research Square

Preprints are preliminary reports that have not undergone peer review.
They should not be considered conclusive, used to inform clinical practice,
or referenced by the media as validated information.

Synergistic Effect of Cu Doping and g-C 3 N 4 /BiVO 4 Heterojunction for Boosted Visible-Light Photocatalytic Degradation of RhB

CuiLin Li

531854054@qq.com

Lanzhou University of Arts and Science

Xiaoyi Meng

Lanzhou University of Arts and Science

Xiaohua Zhao

Lanzhou University of Arts and Science

Shidi Li

Gansu Provincial Education Examinations Authority

Research Article

Keywords: g-C3N4, BiVO4, Cu doping, Heterojunction, Photocatalytic degradation, DFT calculation

Posted Date: October 13th, 2026

DOI: https://doi.org/10.21203/rs.3.rs-11042394/v1

License: This work is licensed under a Creative Commons Attribution 4.0 International License.
Read Full License

Additional Declarations: No competing interests reported.

Synergistic Effect of Cu Doping and g-C_3N_4/$BiVO_4$ Heterojunction for Boosted Visible-Light Photocatalytic Degradation of RhB

Cuilin Li[1*], Xiaoyi Meng[1], Xiaohua Zhao[1] , Shidi Li[2*]

1. College of Chemical Engineering, Lanzhou University of Arts and Science, No. 400 Yanbei Road, Lanzhou, 730000, Gansu, China.

2. Gansu Provincial Education Examinations Authority, No. 399 Yanning Road, Lanzhou, 730000, Gansu, China.

***Correspondence Auther.**

Cuilin Li: Tel.: +86 13919407983. Fax: +86 931 8685568. E-mail: 531854054@qq.com

ORCID: 0009000019996694

Shidi Li: Tel.: +86 18919184169. Fax: +86 931 8583539. E-mail: lishidi1984@163.com

Abstract: The construction of semiconductor heterojunctions combined with elemental doping is a feasible and efficient strategy to optimize the optical properties of photocatalytic materials. In this work, Cu-doped g-C_3N_4/$BiVO_4$ composite photocatalysts were successfully fabricated via a facile synthetic route. Characterization confirmed that $BiVO_4$ nanoparticles uniformly grow on g-C_3N_4 nanosheets, with Cu species coordinating with the triazine ring to form a well-contacted heterojunction interface. Under visible-light irradiation, the optimized Cu/g-C_3N_4/$BiVO_4$ composite achieved a rhodamine B (RhB) degradation efficiency of 92.01% within 60 min, significantly outperforming pure g-C_3N_4, $BiVO_4$, and Cu/g-C_3N_4. In addition, the composite maintains excellent cyclic stability after four

repeated degradation tests, with only a slight decrease in catalytic activity. Radical trapping experiments verify that $\cdot O_2^-$ and h^+ are the dominant active species responsible for RhB photodegradation. To further clarify the intrinsic enhancement mechanism at the atomic level, density functional theory (DFT) calculations were performed. The theoretical results intuitively reveal the electronic structure modulation and interfacial charge transfer behavior induced by Cu doping and heterojunction construction, confirming the establishment of a Type-II charge transfer pathway. The synergistic effect between Cu doping and heterojunction structure effectively broadens the visible-light absorption range and suppresses the recombination of photogenerated carriers. This work clarifies the structure-activity relationship of modified g-C_3N_4-based composites via combined experimental and theoretical investigations, providing a reliable reference for the design and preparation of high-efficiency visible-light photocatalysts.

keywords: g-C_3N_4; $BiVO_4$; Cu doping; Heterojunction; Photocatalytic degradation; DFT calculation

Highlights

1. A Cu-modified g-C_3N_4/$BiVO_4$ composite photocatalyst was prepared through a facile synthetic method, and the well-defined heterojunction structure and successful Cu doping were verified by systematic characterization.

2. The synergistic effect of Cu doping and heterojunction construction endows the Cu/g-C_3N_4/$BiVO_4$ composite with improved visible-light absorption, efficient charge separation and excellent cyclic stability, achieving prominent RhB photodegradation performance.

3. DFT theoretical calculations were applied to analyze the electronic structure, charge distribution and interfacial electron transfer of the composite system, which further elaborates the intrinsic photocatalytic enhancement mechanism.

4. The joint experimental and theoretical study clarifies the structure-activity relationship of g-C_3N_4-based composite photocatalysts, offering feasible guidance for the optimization and design of advanced environmental remediation photocatalysts.

1 Introduction

Semiconductor photocatalysis is considered as a green and sustainable environmental remediation technology, which can efficiently utilize visible solar energy to degrade organic pollutants in water. Benefiting from the advantages of low cost, mild reaction conditions and no secondary pollution, photocatalysis has broad application prospects in wastewater treatment [1-4]. Nevertheless, the practical application of single semiconductor photocatalysts is still restricted by inherent defects, including narrow light response range, low photogenerated charge separation efficiency and rapid electron-hole recombination, which limit the improvement of photocatalytic activity [5-7].

Graphitic carbon nitride (g-C_3N_4), as a typical metal-free visible-light-driven photocatalyst, has attracted extensive research attention due to its stable chemical properties, adjustable structure and simple preparation process. However, pristine g-C_3N_4 suffers from a relatively wide band gap (~2.7 eV) and rapid carrier recombination, which severely restrict its photocatalytic efficiency [8-11]. Bismuth vanadate ($BiVO_4$) is another promising visible-light photocatalyst with a narrow band gap (2.3~2.4 eV) and good visible-light response ability. Whereas, the rapid recombination of photogenerated charges also limits the practical photocatalytic performance of pure $BiVO_4$ [12-14].

Elemental doping and heterojunction engineering are two common and effective modification strategies to solve the above problems. Element doping can regulate the electronic structure of photocatalysts and introduce defect active sites, while heterojunction construction can build valid interfacial charge transfer channels to promote carrier separation. A large number of studies have confirmed that the combination of the two strategies can produce a significant synergistic effect, further optimizing the photocatalytic performance of composite materials [15-21]. For instance, metal ion doping can effectively trap photogenerated electrons and inhibit charge recombination, while the construction of g-C_3N_4/$BiVO_4$ heterojunction can integrate the advantages of the two semiconductors, broaden the light absorption range and optimize interfacial electron transfer [22-25].

Although relevant composite photocatalysts have been reported, the atomic-scale mechanism of the synergistic effect between metal doping and heterojunction interface remains insufficiently elaborated by experimental characterization alone. It is still necessary to combine theoretical calculations to clarify the internal electronic structure evolution and charge transfer mechanism.

In this work, a Cu-doped g-C_3N_4/$BiVO_4$ composite photocatalyst was fabricated by coupling in-situ metal doping and heterojunction construction. The microstructure, optical absorption performance and photoelectrochemical properties of the composites were systematically investigated via multiple characterization methods. Photocatalytic degradation experiments of RhB were carried out to evaluate the catalytic activity and cyclic stability of the samples. More importantly, DFT first-principles calculations were employed to analyze the density of states, differential charge density and work function of the composite system, revealing the intrinsic enhancement mechanism induced by Cu doping and heterojunction formation. The combined experimental and theoretical results systematically clarify the structure-activity relationship of the composite photocatalyst. This study provides effective experimental basis and theoretical support for the modification and performance optimization of g-C_3N_4-based visible-light photocatalysts.

2 Experiments

2.1 Materials

All chemical reagents, specifically urea, $Cu(NO_3)_2$, $Bi(NO_3)_3 \cdot 5H_2O$, NH_4VO_3, HNO_3, NaOH, anhydrous ethanol, RhB, benzoquinone (BQ), ethylenediaminetetraacetate disodium salt (EDTA-2Na), and isopropanol (IPA), were obtained from Macklin Co., Ltd. (China) and used as received.

2.2 Synthesis of g-C_3N_4

The synthesis of ultrathin g-C_3N_4 nanosheets was carried out via thermal polymerization. In a typical procedure, 5 g of urea was placed in a covered crucible and heated to 550 °C at a ramp rate of 13 °C min^{-1} in a muffle furnace. The temperature was held for 4 h, yielding a pale yellow solid. Upon cooling to room

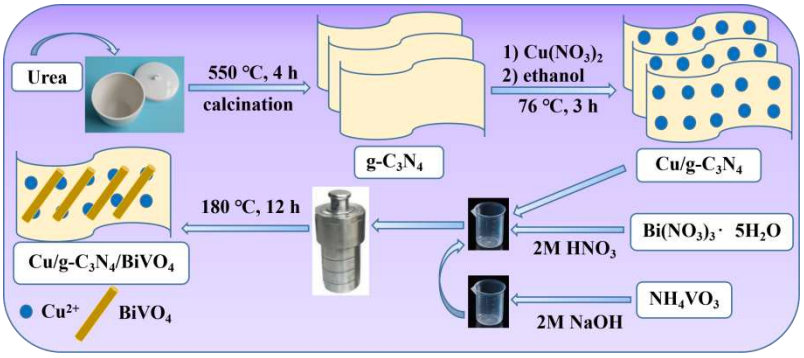
temperature, the product was ground and stored. Compared with traditional methods [26-28], this strategy eliminates the requirement for additional exfoliation treatments (thermal, solvent, or ultrasonic), resulting in a more straightforward and energy-efficient process.

2.3 Synthesis of Cu/g-C_3N_4

The synthesis of Cu/g-C_3N_4 was carried out by a solution-based method. Briefly, 0.3 g of g-C_3N_4 powder was ultrasonically dispersed in 25 mL of anhydrous ethanol, and 0.03 g of $Cu(NO_3)_2$ was then introduced into the dispersion. After sonication for 0.5 h, the mixture was refluxed at 76 °C for 3 h. The resulting solid was separated via centrifugation, washed three times each with 7 mL of distilled water and 7 mL of anhydrous ethanol to remove unreacted copper species, and dried in an oven at 60 °C for 12 h.

2.4 Synthesis of Cu/g-C_3N_4/$BiVO_4$

The synthesis of Cu/g-C_3N_4/$BiVO_4$ was conducted via a hydrothermal method. In detail, 0.5 g of Cu/g-C_3N_4 and 1.225 g of $Bi(NO_3)_3 \cdot 5H_2O$ were dissolved in 20 mL of 2 M HNO_3 to form Solution A, and 0.3 g of NH_4VO_3 was dissolved in 20 mL of 2 M NaOH to form Solution B. Solution B was gradually introduced into Solution A under stirring, followed by pH adjustment to 9 using 0.1 M NaOH. The resulting suspension was sealed in a 100 mL Teflon-lined autoclave and maintained at 180 °C for 12 h. Upon cooling to room temperature, the solid product was separated by centrifugation, washed with deionized water and anhydrous ethanol to eliminate impurities, and dried in an oven at 80 °C for 6 h to obtain a yellow powder (Scheme 1). Pure $BiVO_4$ nanorods were also synthesized under the same conditions but without the addition of Cu/g-C_3N_4.



Scheme 1 Illustration for the synthesis of Cu/g-C_3N_4/$BiVO_4$

2.5 Characterization

Fourier transform infrared (FT-IR) spectra: recorded on a LIDA-20 spectrometer (400-4000 cm^{-1}, KBr disk method). X-ray diffraction (XRD): performed on a Rigaku D/MAX 2400 diffractometer (Cu Kα radiation, 10-80° 2θ, scan rate 5° min^{-1}). Morphology: observed via scanning electron microscopy (SEM, S-4800) and transmission electron microscopy (TEM, TECNAI G2). Chemical states: analyzed via X-ray photoelectron spectroscopy (XPS, Escalab 250Xi, Thermo Fisher), with binding energies calibrated against C 1s (284.8 eV). Optical properties: UV-visible diffuse reflectance spectra (DRS) and absorption spectra recorded on a Shimadzu UV-2600 spectrophotometer; photoluminescence (PL) spectra measured on a FELS-55 spectrofluorometer (excitation wavelength 360 nm). Electrochemical measurements: conducted on a CHI660 electrochemical workstation.

2.6 photocatalytic activity Tests

RhB degradation was performed in a BL-GHX-V photochemical reactor (Shanghai Billang Instrument Co., Ltd.). Typically, 10 mg of catalyst was dispersed in 50 mL of 10 $mg \cdot L^{-1}$ RhB solution, stirred in the dark for 30 min to reach adsorption-desorption equilibrium, then irradiated under visible light. At intervals, 5 mL of suspension was centrifuged, and the absorbance of supernatant was measured at 554 nm (maximum absorption wavelength of RhB) using a UV-visible

spectrophotometer. The degradation efficiency (η) was calculated according to the equation (1):

$$\eta = \left(1 - \frac{A_t}{A_0}\right) \times 100\% \quad (1)$$

where A_0 and A_t are the absorbances of RhB before and after irradiation, respectively.

2.7 Electrochemical measurements

A three-electrode system was used: Ag/AgCl (reference), Pt sheet (counter), and ITO coated with catalyst (working electrode). A 350 W BBZM-III xenon lamp (380-800 nm, Anhui Bobei Lighting) was used as the light source, and 0.2 M Na_2SO_4 was the electrolyte.

3. Calculational models and methods

Density functional theory (DFT) calculations were performed using the GGA + U method (Dudarev's approach) with a U value of 2.0 eV for V 3d states in $BiVO_4$; HSE06 functional was used for g-C_3N_4 (001). A plane-wave basis set with a cut off energy of 400 eV was employed. Monkhorst-Pack k-point meshes of 2×5×1 (for $BiVO_4$, g-C_3N_4/$BiVO_4$, and Cu/g-C_3N_4/$BiVO_4$) and 9×9×1 (for g-C_3N_4) were used for geometric optimization, with residual forces converged to <0.01 eV $Å^{-1}$. A 20 Å vacuum layer was introduced to avoid interlayer coupling. The $BiVO_4$ (010) surface was chosen as the substrate to support the g-C_3N_4 (001) monolayer. The heterostructure was constructed by depositing a relaxed 2√3×1 g-C_3N_4 monolayer onto a relaxed 3×1 $BiVO_4$ (010) surface, ensuring low lattice mismatch (Figure 1).

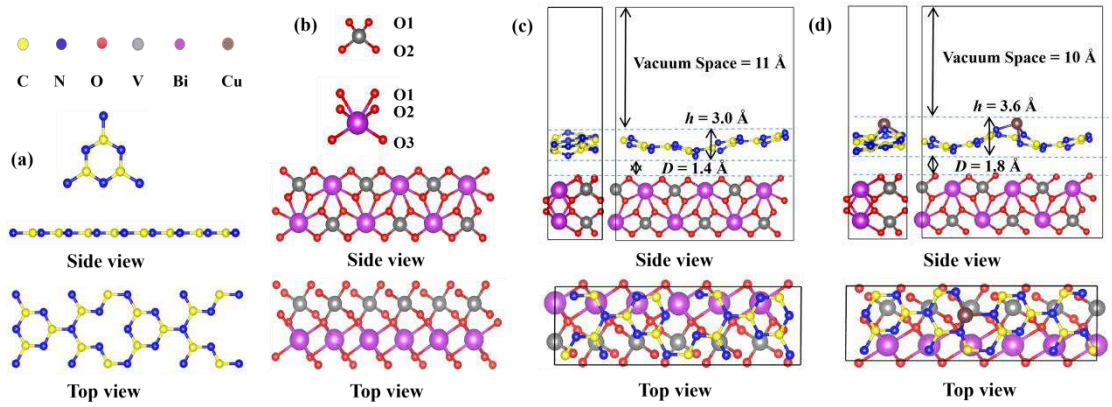


Figure 1 Optimized geometric structures of (a) unit cell of g-C_3N_4 monolayer and 2√3×1 supercell of g-C_3N_4 monolayer, (b) VO_4 and BiO_6 polyhedrons, 3×1 supercell of $BiVO_4$ (010) surface, (c) g-C_3N_4/$BiVO_4$ heterostructure , and (d) Cu/g-C_3N_4/$BiVO_4$ heterostructure.

4 Results and discussion

4.1 Structural and Morphological Analysis

The chemical bonding features of the samples were investigated by FT-IR spectroscopy, as presented in Figure 2a. For pure $BiVO_4$, the absorption bands located at 698 cm^{-1} and 740 cm^{-1} are assigned to the bending vibration of Bi-O bonds, while the peak at 476 cm^{-1} corresponds to the stretching vibration of VO_4^{3-} groups [29]. In the spectrum of g-C_3N_4, a sharp band at 810 cm^{-1} is attributed to the characteristic breathing mode of s-triazine ring units. The band at 890 cm^{-1} arises from N-H bending vibration, the broad absorption in the range of 1230-1650 cm^{-1} is associated with C-N and C=N stretching vibrations within the conjugated framework, and the broad envelope between 3000 and 3350 cm^{-1} originates from N-H stretching of residual -NH_2 groups [30-32]. After Cu incorporation, the Cu/g-C_3N_4 spectrum retains the same peak positions as pristine g-C_3N_4; however, a noticeable decrease in band intensity is detected, suggesting that Cu ions coordinate with nitrogen atoms while the triazine skeleton remains intact [33]. In the case of the Cu/g-C_3N_4/$BiVO_4$ composite,

the coexistence of characteristic absorption bands from both $BiVO_4$ and g-C_3N_4 is clearly observed, which provides strong evidence for the successful construction of the composite.

The crystalline structures of the as-prepared samples were characterized by XRD, as displayed in Figure 2b. For bare g-C_3N_4, two distinct diffraction peaks are observed at 2θ values of 13.1° and 27.7°, which are indexed to the (100) and (002) crystallographic planes, respectively, in good agreement with PDF No. 87-1526 [34,35]. Upon Cu doping, the Cu/g-C_3N_4 pattern preserves the same peak positions; however, the diffraction peaks become weaker and broader compared with those of pristine g-C_3N_4. This behavior can be ascribed to the successful substitution of Cu^{2+} ions into theg-C_3N_4 lattice. Notably, no additional diffraction signals attributable to metallic Cu or copper oxide phases are detected, which is in line with the XPS results [36]. Pure $BiVO_4$ presents a series of well-defined peaks at 18.5°, 19.0°, 28.1°, and other positions, all of which can be readily assigned to the monoclinic scheelite phase of $BiVO_4$ (JCPDS No. 14-0688) [37,38]. For the Cu/g-C_3N_4/$BiVO_4$ composite, the XRD profile contains the characteristic reflections of both g-C_3N_4 and $BiVO_4$ without any impurity phases, verifying the successful fabrication of the heterostructure.

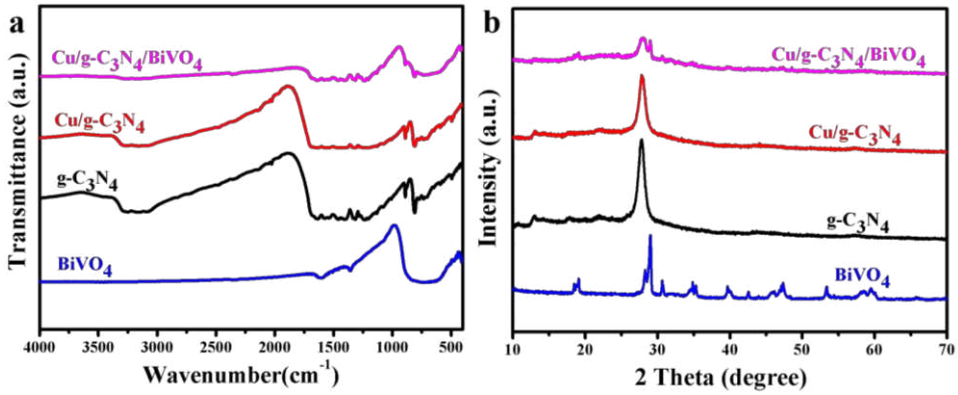


Figure 2 FT-IR spectra (**a**) and XRD patterns (**b**) of $BiVO_4$, g-C_3N_4, Cu/g-C_3N_4 and Cu/g-C_3N_4/$BiVO_4$

As shown in Figures 3a-f, the morphological characteristics of the as-prepared samples were examined by SEM and TEM. Pristine $BiVO_4$ exhibits a well-defined

tetragonal prismatic shape with an average length and width of approximately 5 μm and 1 μm, respectively (Figure 3a). In contrast, bare g-C_3N_4 displays a typical wrinkled two-dimensional sheet-like architecture with irregular folds, which serves as an ideal platform for composite construction (Figure 3b). Upon Cu incorporation, the g-C_3N_4 sheets become fragmented; notably, no discrete Cu nanoparticles are observed on the surface, implying that Cu species are incorporated into the lattice rather than existing as isolated particles (Figure 3c). For the Cu/g-C_3N_4/$BiVO_4$ composite, $BiVO_4$ nanorods with a narrowed width of ~16 nm are uniformly anchored onto the ultrathin g-C_3N_4 sheets (Figure 3d-f). Compared with pure $BiVO_4$, the significantly decreased particle dimensions indicate that the Cu-doped g-C_3N_4 substrate effectively restricts the crystal growth of $BiVO_4$ and enhances its dispersion. Furthermore, TEM analysis verifies the close interfacial contact between the two components, confirming the formation of an intimate heterojunction rather than a simple physical mixture, which is beneficial for efficient charge carrier separation.

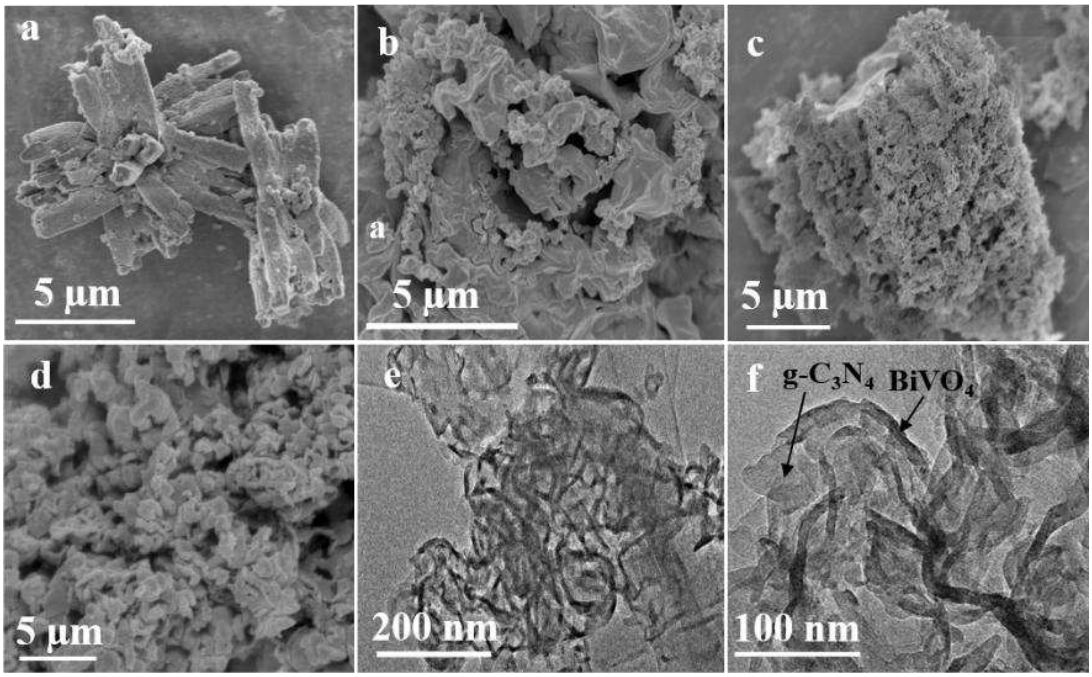


Figure 3 The SEM of $BiVO_4$ (**a**), g-C_3N_4 (**b**), Cu/g-C_3N_4 (**c**) and Cu/g-C_3N_4/$BiVO_4$ (**d**) , the TEM of Cu/g-C_3N_4/$BiVO_4$ (**e, f**)

4.2 Surface Chemical composition (XPS)

XPS survey analysis was performed to determine the surface elemental composition and chemical states of the Cu/g-C_3N_4/$BiVO_4$ composite. As shown in Figure 4a, the survey spectrum clearly displays the characteristic signals of C, N, Bi, V, Cu, and O, confirming the coexistence of all expected elements in the composite.

The high-resolution C 1s spectrum (Figure 4b) can be deconvoluted into two peaks centered at 284.8 eV and 288.2 eV, which are assigned to sp^2 C-C bonds and sp^2 N-C=N bonds within the triazine rings, respectively [39]. The N 1s spectrum (Figure 4c) is fitted into three components: the peak at 398.7 eV corresponds to tertiary nitrogen N-$(C)_3$, the one at 400.4 eV is attributed to C-N=C bonds, and the peak at 404.5 eV originates from C-N-H species [40].

For the Bi 4f region (Figure 4d), two well-resolved peaks are observed at binding energies of 159.6 eV and 164.9 eV, corresponding to Bi $4f_{7/2}$ and Bi $4f_{5/2}$, respectively, which confirms the trivalent state of Bi (Bi^{3+}) [41]. The V 2p spectrum (Figure 4e) exhibits two peaks at 517.0 eV (V $2p_{3/2}$) and 532.0 eV (V $2p_{1/2}$), indicative of V^{5+} [42].

The Cu 2p spectrum (Figure 4f) presents two characteristic peaks at 932.7 eV and 952.6 eV, which are assigned to Cu $2p_{3/2}$ and Cu $2p_{1/2}$, respectively. These binding energies confirm the presence of Cu^{2+} species coordinated with pyridine-type nitrogen and terminal amino groups [43], which is in good agreement with the XRD and TEM findings.

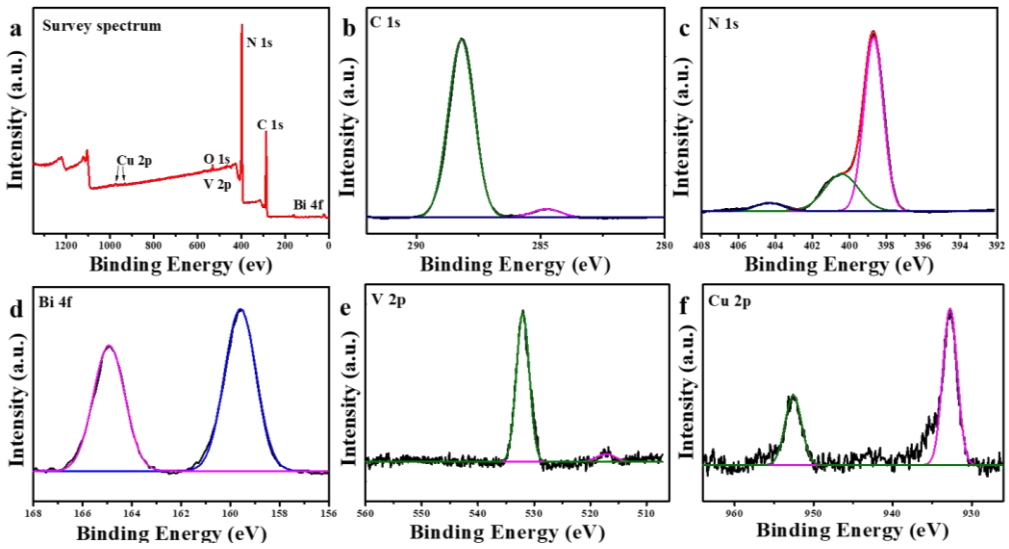


Figure 4 Survey XPS spectra (**a**), C 1s XPS spectra (**b**), N 1s XPS spectra (**c**), Bi 4f XPS spectra (**d**), V 2p XPS spectra (**e**) and Cu 2p XPS spectra (**f**) for Cu/g-C_3N_4/$BiVO_4$

4.3 Optical and Electronic Properties

The optical properties of the samples were investigated by UV-vis diffuse reflectance spectroscopy (DRS), as presented in Figure 5a. Pristine g-C_3N_4 exhibits an absorption edge at approximately 413 nm, indicating a relatively narrow visible-light response range. In contrast, pure $BiVO_4$ displays a significantly red-shifted absorption edge at around 568 nm, demonstrating a broader absorption capability across the visible-light region. Upon Cu incorporation, the absorption edge of Cu/g-C_3N_4 undergoes a slight red shift compared with that of bare g-C_3N_4, which can be attributed to the introduction of intermediate energy levels within the bandgap induced by Cu doping, thereby extending the light-harvesting range [44]. Notably, the Cu/g-C_3N_4/$BiVO_4$ composite shows a further red shift of the absorption edge toward longer wavelengths, approaching that of $BiVO_4$. This result suggests that the coupling of g-C_3N_4 with $BiVO_4$ effectively broadens the spectral response, leading to enhanced visible-light utilization and improved generation of electron-hole pairs.

Photoluminescence (PL) spectroscopy was employed to evaluate the recombination behavior of photogenerated charge carriers, as shown in Figure 5b.

Bare g-C_3N_4 exhibits a strong emission peak centered at approximately 440 nm, suggesting a high recombination rate of electron-hole pairs. After Cu doping, the PL intensity of Cu/g-C_3N_4 is markedly diminished, implying that the introduction of Cu species effectively suppresses charge recombination by facilitating charge migration. More importantly, the Cu/g-C_3N_4/$BiVO_4$ composite displays a substantially weakened PL signal, which can be ascribed to the synergistic interaction between Cu doping and the formation of a heterojunction interface, both of which collaboratively hinder the recombination process. This observation is well consistent with the enhanced photocatalytic performance of the composite [45].

To determine the bandgap energies (E_g) of the samples, Tauc plots were constructed based on the equation (2) [46,47]:

$$(ah\nu)^{2/n}=A\left(h\nu-E_g\right) \quad (2)$$

where α represents the absorption coefficient, hν denotes the photon energy, A is a proportionality constant, and n takes a value of 1/2 or 2 for direct and indirect optical transitions, respectively. From the Tauc plots (Figure 5c-d), the bandgap values are estimated to be 2.80 eV for g-C_3N_4 and 2.35 eV for $BiVO_4$.

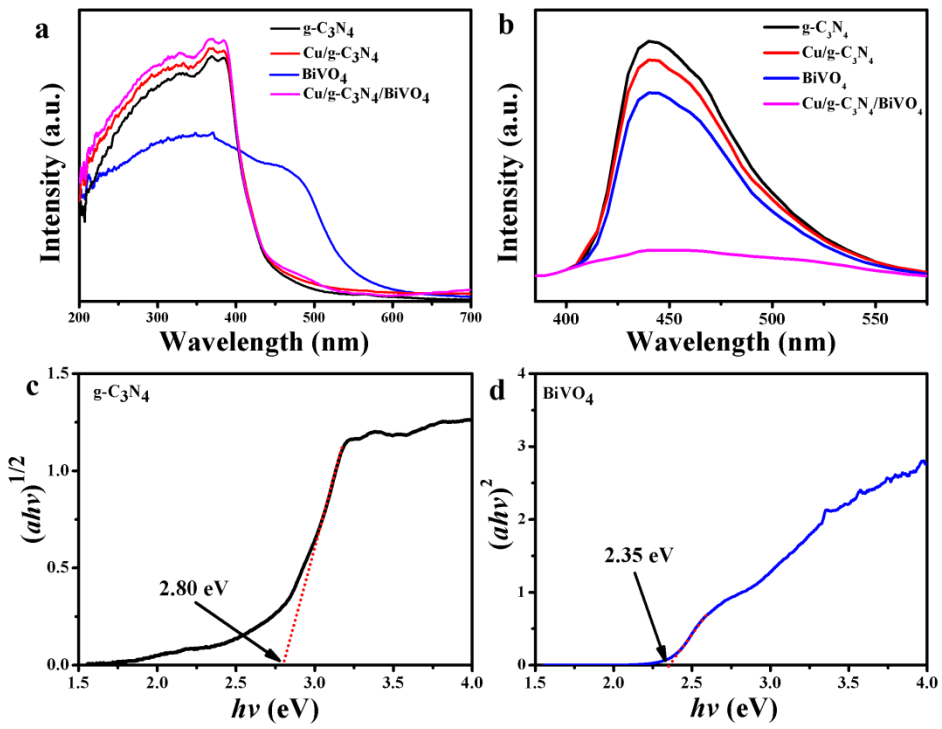


Figure 5 DRS (**a**) and PL (**b**) spectra of g-C_3N_4, Cu/g-C_3N_4, $BiVO_4$ and Cu/g-C_3N_4/$BiVO_4$,Tauc plots of g-C_3N_4 (**c**) and $BiVO_4$ (**d**)

Electrochemical impedance spectroscopy (EIS) measurements were conducted to probe the charge transfer dynamics at the electrode-electrolyte interface. As depicted in Figure 6a, the Nyquist plot of the Cu/g-C_3N_4/$BiVO_4$ composite displays the smallest semicircular arc among all the tested samples, corresponding to the lowest charge transfer resistance (Rct) and thus the most efficient charge separation and transfer capability [48]. This enhanced performance can be rationalized by two key factors: first, the incorporation of Cu species effectively lowers the surface energy barrier, thereby accelerating electron transport kinetics; second, the establishment of a heterojunction interface between g-C_3N_4 and $BiVO_4$ provides an efficient pathway for charge separation, which significantly suppresses the recombination of photogenerated carriers.

Furthermore, transient photocurrent responses were recorded to assess the charge separation efficiency under illumination (Figure 6b). The Cu/g-C_3N_4/$BiVO_4$

composite delivers the highest photocurrent density compared with the individual components, providing direct evidence for its superior electron-hole separation ability [49]. The remarkable enhancement can be attributed to the synergistic interplay between Cu doping and heterojunction construction, which collectively prolong the carrier lifetime and thereby boost the overall photocatalytic activity.

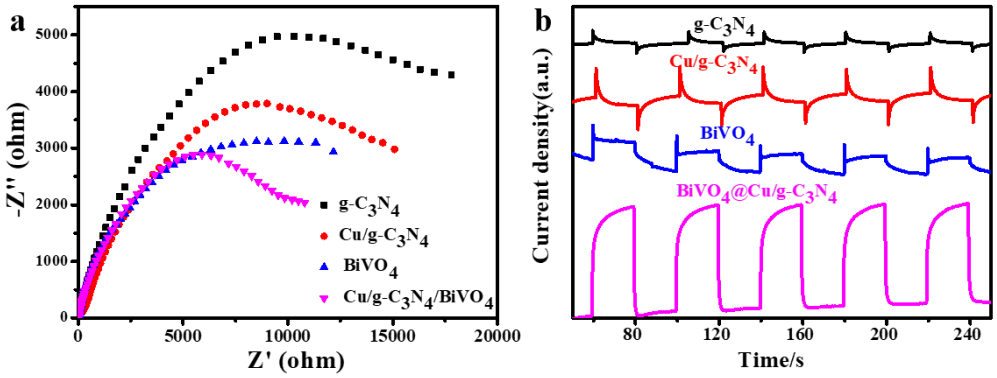


Figure 6 EIS (**a**) and photocurrent response curves of g-C_3N_4, Cu/g-C_3N_4, $BiVO_4$ and Cu/gC_3N_4/$BiVO_4$ (**b**)

4.4 Photocatalytic Performance

The photocatalytic activity of the as-prepared samples was assessed by monitoring the degradation of RhB under visible-light irradiation ($\lambda > 420$ nm). As displayed in Figure 7a, the individual $BiVO_4$, g-C_3N_4, and Cu/g-C_3N_4 samples show limited degradation performance, achieving removal efficiencies of only 18.4%, 36.0%, and 49.1%, respectively, after 60 min of irradiation. Remarkably, the Cu/g-C_3N_4/$BiVO_4$ composite exhibits a significantly enhanced degradation efficiency of 92.02% within the same duration, which is approximately 2.64, 1.76, and 1.30 times greater than that of $BiVO_4$, g-C_3N_4, and Cu/g-C_3N_4, respectively. Moreover, a blank control experiment confirmed that negligible RhB decomposition occurred in the absence of a photocatalyst under natural light, ruling out the contribution of direct photolysis.

These findings are well consistent with the aforementioned characterization results obtained from UV-vis DRS, PL, EIS, and transient photocurrent responses, collectively demonstrating that the synergistic interaction among Cu, $BiVO_4$, and g-C_3N_4 effectively promotes the utilization of photogenerated charge carriers in the degradation process. Consequently, the Cu/g-C_3N_4/$BiVO_4$ composite serves as a highly efficient bifunctional photocatalyst with outstanding photocatalytic performance.

The photocatalytic degradation kinetics of RhB in aqueous solution were further investigated, and the corresponding results are presented in Figure 7b. For all the tested photocatalysts, including $BiVO_4$, g-C_3N_4, Cu/g-C_3N_4, and Cu/g-C_3N_4/$BiVO_4$, a linear relationship is observed between $\ln(A_t/A_0)$ and the irradiation time, indicating that the photodegradation process can be well described by a pseudo-first-order kinetic model [49]. The apparent rate constant (k) for RhB degradation over the Cu/g-C_3N_4/$BiVO_4$ composite is calculated to be 0.08225 min^{-1}, which is approximately 6.10, 3.50, and 2.14 times greater than those of pure $BiVO_4$(0.01349 min^{-1}), g-C_3N_4 (0.02349 min^{-1}), and Cu/g-C_3N_4 (0.03842 min^{-1}), respectively. Such a remarkable enhancement in the reaction rate constant further verifies that the integration of Cu doping with the g-C_3N_4/$BiVO_4$ heterojunction architecture plays a crucial role in boosting the visible-light-driven catalytic performance.

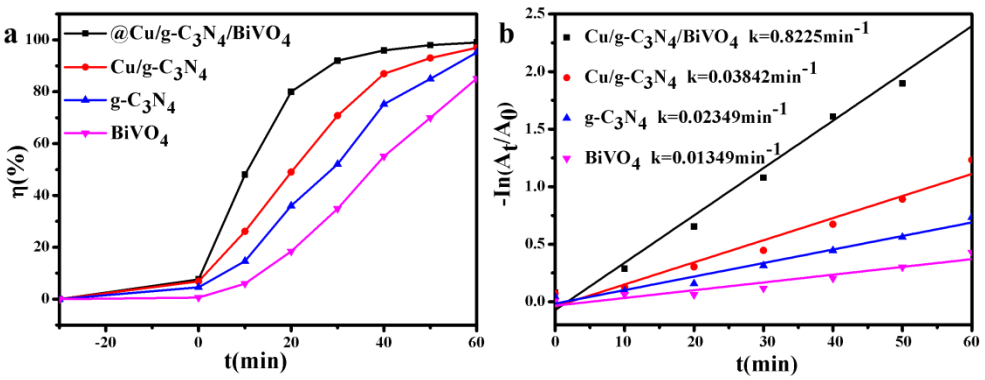


Figure 7 Photocatalytic activities of different photocatalysts based on the photocatalytic degradation of RhB (**a**); Kinetic rate constants of RhB degradation over different photocatalysts (**b**)

The reusability and long-term stability of Cu/g-C_3N_4/$BiVO_4$ composite were evaluated by performing successive photocatalytic degradation experiments under the same reaction conditions. As shown in Figure 8a, the degradation efficiency of RhB undergoes only a slight decrease of 3.99% after four consecutive cycles, demonstrating the favorable recyclability of the catalyst. To further verify the structural integrity of the composite after the photocatalytic reaction, FT-IR and XRD characterizations were carried out on the used sample (Figure 8b and 8c). The results reveal that no discernible changes are observed in the chemical bonding features and crystalline phase of the composite, confirming that Cu/g-C_3N_4/$BiVO_4$ possesses excellent structural stability during the photocatalytic process.

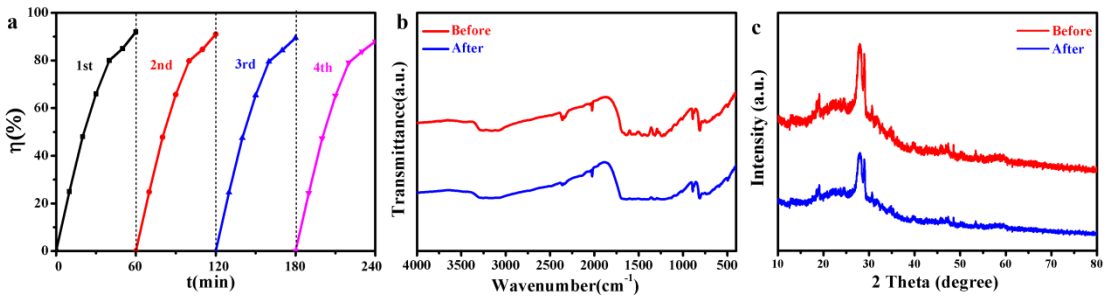


Figure 8 Cyclic stability (**a**), FT-IR spectra (**b**) and XRD patterns (**c**) comparison before and after four cycles of Cu/g-C_3N_4/$BiVO_4$.

4.6 Determination of active species

To identify the dominant reactive species responsible for RhB degradation, free radical scavenging experiments were carried out. Three quenching agents, namely benzoquinone (BQ), ethylenediaminetetraacetate (EDTA-2Na), and isopropanol (IPA), were introduced at a concentration of 1 mmol/L to selectively trap $\cdot O_2^-$, h^+ and·OH radicals, respectively [50,51]. As illustrated in Figure 9, the addition of BQ leads to a dramatic suppression of RhB degradation, with the removal efficiency dropping

sharply from 92.1% to 26.4% within 60 min. Similarly, the introduction of EDTA-2Na also causes a notable decline in degradation performance, reducing the efficiency to 63.7%. In contrast, the photodegradation activity is barely affected upon the addition of IPA, suggesting that ·OH radicals contribute minimally to the reaction. Based on these observations, it can be concluded that $\cdot O_2^-$ and h^+ serve as the primary active species in the photocatalytic degradation of RhB, among which $\cdot O_2^-$ exerts a more dominant role than h^+.

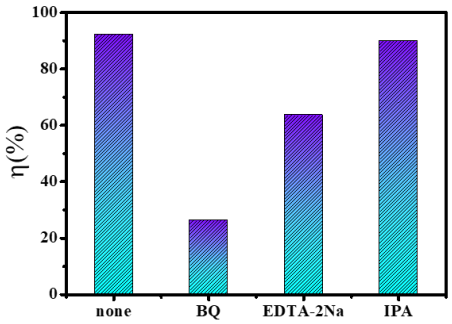


Figure 9 Effect of different free radical agents on the photocatalytic degradation rate of RhB by $Cu/g\text{-}C_3N_4/BiVO_4$

5 Calculation results

5.1 density of states (DOS)

To elucidate the charge-carrier transfer mechanism at the $g\text{-}C_3N_4$ (001)/$BiVO_4$ (010) interface, the total density of states (TDOS) and partial density of states (PDOS) were calculated for $g\text{-}C_3N_4$ (001), $Cu/g\text{-}C_3N_4$, the $BiVO_4$ (010) surface, the $g\text{-}C_3N_4$ /$BiVO_4$ heterostructure, and the $Cu/g\text{-}C_3N_4$ /$BiVO_4$ nanocomposite, as shown in Figure 10. For all calculations, the Fermi level was aligned to the highest occupied state and set to zero [52].

As displayed in Figure 10a and 10a′, the TDOS and PDOS of the $g\text{-}C_3N_4$ (001) surface reveal that the valence band maximum (VBM) is predominantly composed of

N 2p states, whereas the conduction band minimum (CBM) arises from nearly equal contributions of N 2p and C 2p orbitals. The calculated bandgap of approximately 2.9 eV is in good agreement with previously reported values.

For the $BiVO_4$ (010) surface (Figure 10c and 10c′), the computed bandgap is 2.36 eV, which is consistent with both experimental and theoretical results in the literature. The VBM is mainly governed by O 2p states, while the CBM is largely derived from V 3d states. This indicates that the optical absorption of $BiVO_4$ is primarily associated with electron transitions from O 2p to V 3d states, which agrees well with earlier theoretical investigations.

After the formation of the g-C_3N_4/$BiVO_4$ heterostructure (Figure 10d and 10d′), the bandgap decreases to 2.21 eV, which can be attributed to the van der Waals (vdW) interactions between the $BiVO_4$ (010) surface and the g-C_3N_4 monolayer. In this heterostructure, both the CBM and VBM of $BiVO_4$ (010) are located at higher energy levels than those of g-C_3N_4, resulting in a staggered (Type-II) band alignment. Such a band configuration is favorable for suppressing electron-hole recombination and prolonging the lifetime of charge carriers, thereby contributing to improved photocatalytic performance.

Notably, the introduction of Cu leads to further bandgap narrowing. The calculated bandgaps of Cu/g-C_3N_4 and Cu/g-C_3N_4/$BiVO_4$ are 1.56 eV and 1.24 eV, respectively (Figure 10b and 10e). This reduction originates from the involvement of Cu 3d states, which induce a downward shift of the CBM (Figure 10b′and 10e′). A narrower bandgap facilitates the generation of more photoexcited carriers and

enhances visible-light absorption, thereby endowing the Cu/g-C_3N_4/$BiVO_4$ heterostructure with stronger redox capability.

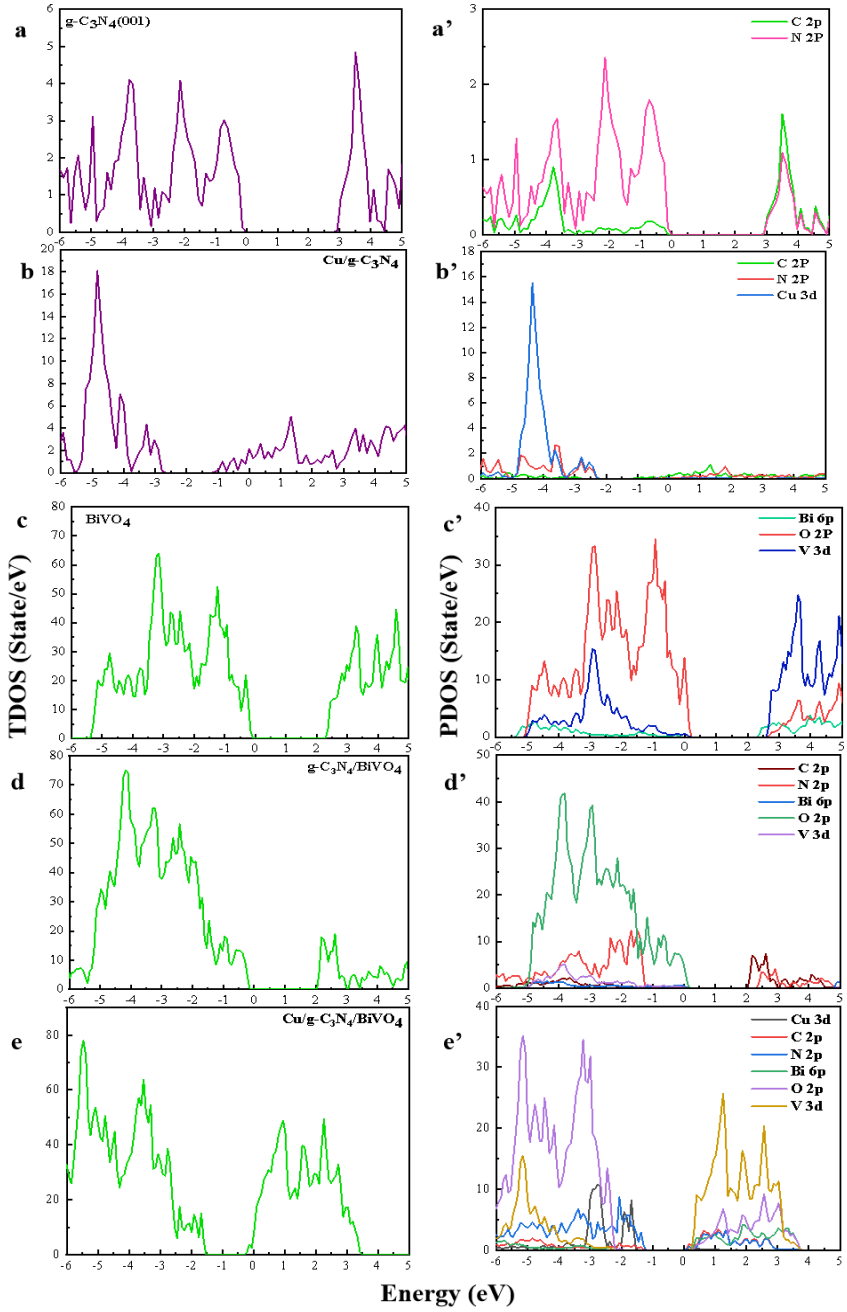


Figure 10 The calculated TDOS and PDOS of g-C_3N_4 (001) surface (a and a'), Cu/g-C_3N_4 surface (b and b'), $BiVO_4$ (010) surface (c and c'), g-C_3N_4/$BiVO_4$ heterostructure(d and d') and Cu/g-C_3N_4/$BiVO_4$ heterostructure (e and e').

5.2 difference charge density

The differential charge density analysis was employed to visualize the interfacial charge redistribution within the heterostructure [53]. The planar-averaged charge density differences along the x-y plane were computed for both the pristine and Cu-doped g-C_3N_4/$BiVO_4$ heterostructures, and the corresponding results are displayed in Figure 11. In these plots, the yellow and cyan isosurfaces represent regions of electron accumulation and electron depletion, respectively.

For the g-C_3N_4 monolayer, the charge density difference is dominated by cyan regions with only sparse yellow areas, indicating substantial electron depletion and the formation of hole-rich zones. In contrast, the $BiVO_4$ (010) surface exhibits predominantly yellow isosurfaces accompanied by minor cyan regions, signifying electron accumulation and the creation of electron-rich sites. Upon visible-light irradiation, photogenerated electrons tend to migrate toward the conduction band (CB) of $BiVO_4$ (010), while holes are retained in the valence band (VB) of g-C_3N_4, thereby realizing efficient spatial charge separation. This charge redistribution is driven by the built-in electric field established at the heterointerface, which directs the migration of electrons and holes between the two components.

Notably, compared with the pristine g-C_3N_4/$BiVO_4$ system, the Cu/g-C_3N_4/$BiVO_4$ heterojunction displays a more pronounced degree of electron transfer, suggesting that Cu doping further facilitates the separation and migration of photogenerated charge carriers. These results confirm that the construction of the g-C_3N_4/$BiVO_4$ heterostructure, combined with Cu incorporation, effectively promotes interfacial charge transfer, suppresses electron-hole recombination, and ultimately

enhances the photocatalytic performance.

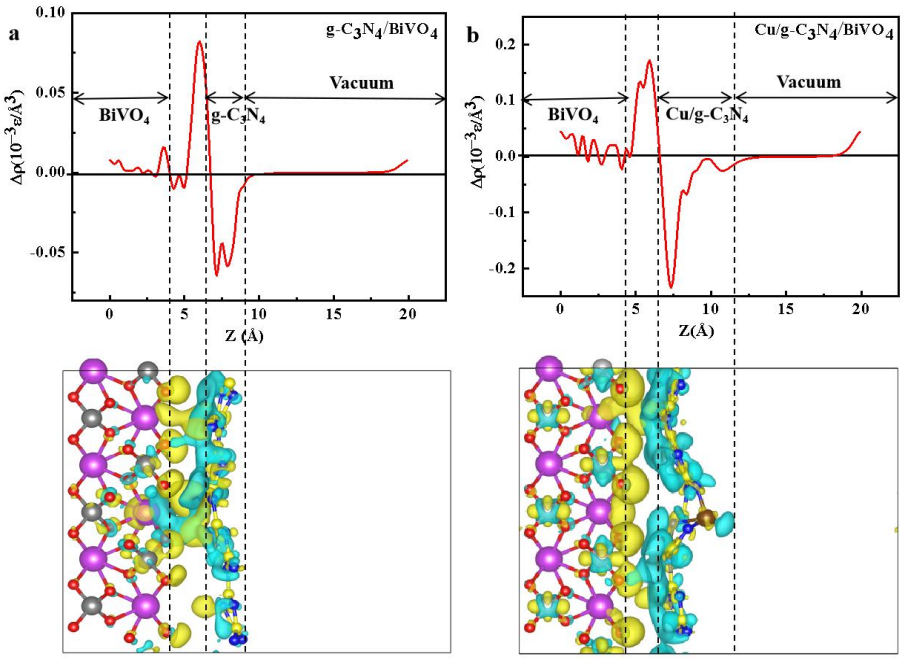


Figure 11 Planar-averaged charge density difference for (a) g-C_3N_4/$BiVO_4$, and (b) Cu/g-C_3N_4/$BiVO_4$ heterostructures.

5.3 Work function

The work function is defined as the minimum energy needed to remove an electron from the Fermi level to the vacuum level. The calculated work functions for the $BiVO_4$ (010) surface, g-C_3N_4 monolayer, g-C_3N_4/$BiVO_4$ heterostructure, and Cu/g-C_3N_4/$BiVO_4$ heterostructure are presented in Figure 12. The g-C_3N_4 monolayer and $BiVO_4$ (010) surface exhibit work functions of 4.06 eV and 7.04 eV, respectively, which are in good agreement with previously reported theoretical values [54]. Given that $BiVO_4$ (010) possesses a higher work function than g-C_3N_4, electrons are thermodynamically favored to migrate from the g-C_3N_4 monolayer to the $BiVO_4$ (010) surface upon contact. Importantly, the work function of the Cu/g-C_3N_4/$BiVO_4$

heterostructure is calculated to be 4.47 eV, which is considerably lower than that of the pristine g-C_3N_4/$BiVO_4$ system (5.60 eV). This reduction suggests that Cu doping facilitates electron emission, thereby promoting charge transfer at the heterointerface.

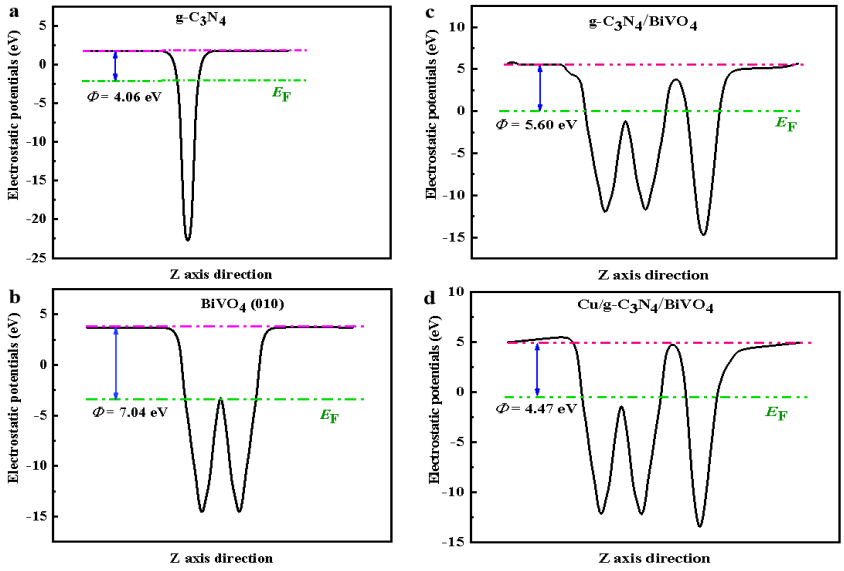


Figure 12 Work functions of (a) g-C_3N_4 monolayer, (b) $BiVO_4$ (010) surface, (c) g-C_3N_4/$BiVO_4$, and (d) Cu/g-C_3N_4/$BiVO_4$ heterostructures.

5.4 Band Edge Potentials

The band edge positions were determined based on the electronegativity (X) and the energy of free electrons (E_e) using the equations (3) and (4) [55]:

$$E_{CB}=X-E_e-E_g/2 \quad (3)$$

$$E_{VB}=E_{CB}+E_g \quad (4)$$

where E_e is the energy of free electrons on the hydrogen scale (E_e = 5.5 eV) [56]. The calculated results are summarized in Table 1.

Table 1 Electronegativity, band gap, conduction band and valence band of g-C_3N_4 and $BiVO_4$

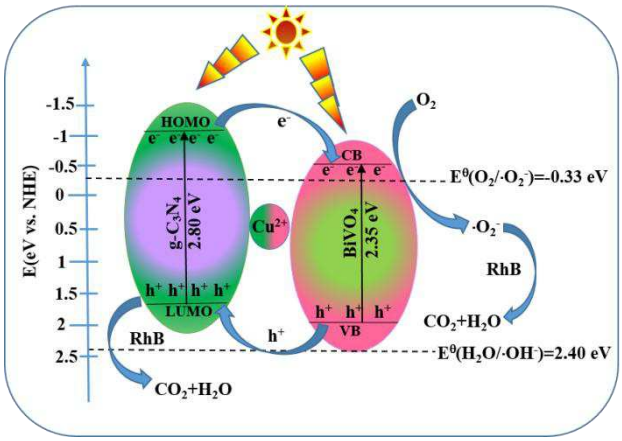
Semiconductor	X (eV)	E_g (eV)	E_{CB} (eV)	E_{VB} (eV)
g-C_3N_4	5.67	2.90	-1.28	1.62
$BiVO_4$	6.16	2.36	-0.52	1.84

5.5 Photocatalytic mechanism

On the basis of the aforementioned results, a plausible photocatalytic mechanism is proposed and illustrated in Scheme 2. Under visible-light irradiation, photogenerated electrons in the conduction band (CB) of g-C_3N_4 are rapidly injected into the CB of $BiVO_4$, while holes in the valence band (VB) of $BiVO_4$ migrate to the VB of g-C_3N_4. Consequently, electrons accumulate in the CB of $BiVO_4$ and holes gather in the VB of g-C_3N_4, achieving efficient spatial charge separation.

Given that the CB potential of $BiVO_4$ (-0.52 eV vs. NHE) is more negative than the $O_2/\cdot O_2^-$ redox potential (-0.33 eV vs. NHE) [57], the accumulated electrons in the $BiVO_4$ CB are thermodynamically capable of reducing dissolved O_2 to produce $\cdot O_2^-$ radicals. On the other hand, the VB potential of g-C_3N_4 (+1.66 eV vs. NHE) is less positive than the $OH^-/\cdot OH$ (+2.40 eV vs. NHE) and $H_2O/\cdot OH$ (+2.72 eV vs. NHE) redox potentials [58], indicating that the holes in the g-C_3N_4 VB are insufficient to oxidize OH^- or H_2O into ·OH radicals. Instead, these holes directly attack the RhB molecules, leading to their progressive degradation into CO_2 and H_2O.

Overall, the outstanding photocatalytic performance of the Cu/g-C_3N_4/$BiVO_4$ composite can be attributed to the Type-II heterojunction formed between $BiVO_4$ and g-C_3N_4, which facilitates the effective separation and transfer of photogenerated electron-hole pairs while broadening the visible-light absorption range. Moreover, the incorporated Cu ions serve as electron transport mediators that accelerate electron migration to the catalyst surface, suppress charge-carrier recombination, and further enhance the overall photocatalytic efficiency.



Scheme **2** Proposed photocatalytic degradation mechanism of RhB under visible light irradiation with Cu/g-C_3N_4/$BiVO_4$ composite.

6 Conclusion

In this work, Cu/g-C_3N_4/$BiVO_4$ composite photocatalyst was successfully prepared via a combination of Cu ion doping and heterojunction construction. Structural and morphological characterizations verify that the introduced Cu ions effectively coordinate with the conjugated triazine ring units of g-C_3N_4 while maintaining its inherent structural framework. Tetragonal $BiVO_4$ nanoparticles are uniformly immobilized on g-C_3N_4 nanosheets, which enriches surface active sites and forms intimate interfacial contacts, both of which facilitate the transfer and separation of photogenerated charges. Photoelectrochemical results confirm that the synergistic coupling of Cu doping and g-C_3N_4/$BiVO_4$ heterojunction optimizes the optical and electrochemical properties of the composite, broadening the visible-light absorption range and improving the separation, migration and utilization efficiency of photogenerated carriers.

Photocatalytic degradation tests toward RhB show that the optimized Cu/g-C_3N_4/$BiVO_4$ composite achieves a degradation efficiency of 92.01% within 60

min for 10 mg/L RhB solution. Its photocatalytic activity is 2.64, 1.76, and 1.30 times higher than that of pure $BiVO_4$, pristine g-C_3N_4, and Cu/g-C_3N_4, respectively. After four cyclic degradation experiments, the composite retains 88.02% of its initial catalytic performance, demonstrating good recyclability and structural stability. Radical trapping measurements indicate that $\cdot O_2^-$ and h^+ serve as the predominant active species dominating the photocatalytic degradation process.

First-principles calculations, including density of states, differential charge density, and work function analyses, were carried out to investigate the electronic structure, interatomic interactions, and charge transfer behavior. The computational results are well consistent with the experimental observations, confirming that Cu doping and $BiVO_4$ heterojunction formation synergistically boost the photocatalytic activity of g-C_3N_4. Together, the experimental and theoretical findings suggest that a Type-II heterojunction is established between $BiVO_4$ and g-C_3N_4. The interfacial conjugation and electrostatic interactions give rise to a well-defined heterointerface, which enlarges the specific surface area, lowers the charge transfer resistance, and promotes efficient electron-hole separation. The enhanced photocatalytic performance is therefore attributed to the increased active sites, extended visible-light absorption, and improved charge separation efficiency, collectively endowing Cu/g-C_3N_4/$BiVO_4$ with high activity and stability toward RhB degradation. This study offers a promising strategy for the rational design of cost-effective and high-performance g-C_3N_4-based visible-light photocatalysts.

Acknowledgments

The authors acknowledge the financial support received from the Gansu Provincial Higher Education Teaching Reform Research Project of 2025 (Grant No.

GJJGB360), the Lanzhou University of Arts and Science Start-up Foundation for Doctoral Research (Grant No. 202007) and the Fund Project for Young Ph.D. in Higher Education Institutions of Gansu Province (Grant No. 2022QB-193).

The authors gratefully acknowledge the use of DeepSeek, Doubao (by ByteDance), and Qwen for English language polishing of this manuscript. The reference formatting was standardized using Qwen.

Authors Contribution statement

Cuilin Li: Conceptualization, Investigation, Writing - original draft;

Shidi Li: Investigation, Writing-review and editing;

Xiaoyi Meng: Software, Formal analysis, Visualization;

Xiaohua Zhao: Investigation .

Declarations Ethical Approval

This study does not involve any experiments on human participants or animals; therefore, ethical approval was not required.

Conflict of Interest

The authors declare that they have no competing financial interests or personal relationships that could be perceived as influencing the work presented in this paper.

Funding

This research did not receive any specific grant from funding agencies in the public, commercial, or not-for-profit sectors.

Availability of data and materials

All data supporting the findings of this study are included within the article.

References

[1] C.D. Menelisi, S.M. Manoko, A.M. John, The use of TiO_2/clay heterostructures in the photocatalytic remediation of water containing organic pollutants: a review, J. Environ. Chem. Eng. 9 (2021) 106546. https://doi.org/10.1016/j.jece.2021.106546.

[2] A.S. Al-Wasidi, F.A. Saad, S. Alreshaidan, et al., Facile synthesis of ZSM-5/TiO_2/Ni novel nanocomposite for the efficient photocatalytic degradation of methylene blue dye, J. Inorg. Organomet. Polym. Mater. 32 (2022) 3040-3052. https://doi.org/10.1007/s10904-022-02336-7.

[3] S. Natarajan, H.C. Bajaj, R.J. Tayade, Recent advances based on the synergetic effect of adsorption for removal of dyes from waste water using photocatalytic process, J. Environ. Sci. 65 (2018) 201-222. https://doi.org/10.1016/j.jes.2017.03.011.

[4] S. Mancipe, J. Martinez, C. Pinzon, et al., Effective photocatalytic degradation of Rhodamine B using tin semiconductors over hydrotalcite-type materials under sunlight driven, Catal. Today 372 (2021) 191-197. https://doi.org/10.1016/j.cattod.2020.12.014.

[5] Y. Liu, P. Li, Y. Liu, et al., Recent advances in carbon dots as a single photocatalyst, Acta Phys.-Chim. Sin. 42 (2026) 100167. https://doi.org/10.1016/j.actphy.2025.100167.

[6] A. Kurian, S. Shanmugam, Spinel aluminate-based heterojunctions as photocatalyst: a review, Chem. Open 15 (2026) e202500473. https://doi.org/10.1002/open.202500473.

[7] S. Ji, Y. Zhang, L. Shi, The improved photocatalytic performance over $Cu_{2-x}S/Cd_xMn_{1-x}S$ hollow cube S-scheme heterojunction photocatalyst, J. Photochem. Photobiol. A 473 (2026) 116884. https://doi.org/10.1016/j.jphotochem.2025.116884.

[8] X. Song, G. Yuan, X. Wang, Sulfur doping and S-scheme heterojunction construction synergistically enhance the photocatalytic performance of g-C_3N_4, Sol. Energy 303 (2026) 114127. https://doi.org/10.1016/j.solener.2025.114127.

[9] Y. Shi, X. Wang, Z. Su, et al., The degradation mechanism of $BiFe_{0.98}Al_{0.02}O_3$-$BaTiO_3$/g-C_3N_4/Cu II-type heterojunction induced by synergistic effect of piezoelectric and illuminant, J. Mater. Sci. 61 (2026) 17141-17159. https://doi.org/10.1007/s10853-026-12857-y.

[10] Y. Zhang, J.S. Yuan, Y.J. Ding, B. Liu, L. Zhao, S.G. Zhang, Research progress on g-C_3N_4-based photocatalysts for organic pollutants degradation in wastewater: from exciton and carrier perspectives, Ceram. Int. 47 (2021) 31005-31030. https://doi.org/10.1016/j.ceramint.2021.08.063.

[11] M. Ahmaruzzaman, S.R. Mishra, Photocatalytic performance of g-C_3N_4 based nanocomposites for effective degradation/removal of dyes from water and wastewater, Mater. Res. Bull. 143 (2021) 111417. https://doi.org/10.1016/j.materresbull.2021.111417.

[12] F.R.S. Mohamad, S. Suriati, B.H. Hameed, Epigrammatic progress and perspective on the photocatalytic properties of BiVO4-based photocatalyst in photocatalytic water treatment technology: a review, J. Mol. Liq. 268 (2018) 438-459. https://doi.org/10.1016/j.molliq.2018.07.051.

[13] P. Wua, S. Attarde, C.C. Lu, et al., $ZnMn_2O_4$-$BiVO_4$ as photocatalyst for degradation of gaseous HCHO using daylight, Chem. Sel. 9 (2024) e202401501. https://doi.org/10.1002/slct.202401501.

[14] M. Ashokkumar, P. Arunachalam, A review on $BiVO_4$ photocatalyst: activity enhancement methods for solar photocatalytic applications, Appl. Catal. A 555 (2018) 47-74. https://doi.org/10.1016/j.apcata.2018.02.010.

[15] A. Aishwarya, A.P. Chowdhury, K.S. Anantharaju, et al., Dual S-scheme Ag_3PO_4/$CoWO_4$/g-C_3N_4 ternary nanocomposite for photo degradation of Rhodamine B pollutant and electrochemical detection of acetaminophen, J. Water Process Eng. 82 (2026) 109421. https://doi.org/10.1016/j.jwpe.2025.109421.

[16] P.P. Gotipamul, G. Vattikondala, K.D. Rajan, et al., Impact of piezoelectric effect on the heterogeneous visible photocatalysis of g-C_3N_4/Ag/ZnO tricomponent, Chemosphere 287 (2022) 132298. https://doi.org/10.1016/j.chemosphere.2021.132298.

[17] J. Cao, J. Cai, R. Li, et al., A novel 3D yolk-double-shell Au@CdS/g-C_3N_4 nanostructure with enhanced photoelectrochemical and photocatalytic properties, J. Phys. Chem. C 126 (2022) 4939-4947. https://doi.org/10.1021/acs.jpcc.1c09841.

[18] C. Li, Q. Zhai, W. Liu, et al., Facile fabrication of CdS/Cu-doped g-C_3N_4 heterojunction for enhanced photocatalytic degradation of methylene blue, J. Mater. Sci.: Mater. Electron. 34 (2023) 1659. https://doi.org/10.1007/s10854-023-11055-9.

[19] C. Yavuz, S. Erten-Ela, Solar light-responsive α-Fe_2O_3/CdS/g-C_3N_4 ternary photocatalyst for photocatalytic hydrogen production and photodegradation of methylene blue, J. Alloys Compd. 908 (2022) 164584. https://doi.org/10.1016/j.jallcom.2022.164584.

[20] W.E. Mouhri, I. Nadif, N. Tajat, et al., Mechanochemical synthesis of AgI–BiOI@g-C_3N_4 heterojunction for the efficient degradation of cationic dye RhB under visible light irradiation, J. Phys. Chem. Solids 208 (2026) 113013. https://doi.org/10.1016/j.jpcs.2025.113013.

[21] P. Lai, J. Li, Z. Xu, et al., In-situ constructed Z-scheme $Bi_2O_2CO_3$/g-C_3N_4 heterojunction: enhanced photocatalytic degradation of preservatives, Sep. Purif. Technol. 382 (2026) 135892. https://doi.org/10.1016/j.seppur.2025.135892.

[22] X. Zhang, S. Jia, J. Ma, et al., Cobalt-doped g-C_3N_4/CoO S-scheme heterojunction enabling efficient photothermal CO_2 conversion via synergistic charge transfer and reaction pathway regulation, J. Colloid Interface Sci. 702 (2026) 138996. https://doi.org/10.1016/j.jcis.2025.138996.

[23] S. Le, T. Jiang, Q. Zhao, et al., Cu-doped mesoporous graphitic carbon nitride for enhanced visible-light driven photocatalysis, RSC Adv. 6 (2016) 38811-38819. https://doi.org/10.1039/C6RA03982K.

[24] P. Mohan, S. Mallapur, S.G. Kumar, Integrating the bicrystalline monoclinic-tetragonal $BiVO_4$ with g-C_3N_4 to form S-scheme heterojunction for bromocresol green dye degradation under visible light, J. Mater. Sci.: Mater. Electron. 37 (2026) 180. https://doi.org/10.1007/s10854-025-16555-4.

[25] P.K. Panda, R. Pattanaik, D. Pradhan, et al., Enhanced solar light driven remediation of toxic dye contaminated water using strontium doped $BiVO_4$/g-C_3N_4 with mechanistic insights and kinetic evaluation, Discover Mater. 6 (2026) 68. https://doi.org/10.1007/s43939-026-00560-3.

[26] M.A. Ahmed, S.A. Mahmoud, A.A. Mohamed, Unveiling the photocatalytic potential of graphitic carbon nitride (g-C_3N_4): a state-of-the-art review, RSC Adv. 14(2024) 25629-25663. https://doi.org/10.1039/d4ra04234d.

[27] M.A. Nazir, M. Salih, O.P. Kumar, et al., Synergistic photocatalysis via G-C_3N_4/ZIF-8 S-scheme heterojunction: a strategy for superior pollutant degradation, Chem. Cat. Chem. 18 (2026) e70886. https://doi.org/10.1002/cctc.70886.

[28] W. Wang, M. Zhang, B. Zhao, et al., Synthesis of Bi_2WO_6/g-C_3N_4 photocatalyst and high degradation of Rhodamine B under visible light irradiation, Pigm. Resin Technol. 51 (2022) 91-100. https://doi.org/10.1108/PRT-09-2020-0097.

[29] M. Kaur, P. Hait, S. Basu, Flower-like NiAl-LDH/$BiVO_4$ Z-scheme photocatalysts for sunlight-driven degradation of azo dye: performance and mechanistic insights, RSC Adv. 15 (2025) 37166-37182. https://doi.org/10.1039/d5ra06146f.

[30] M.I. Nabeel, N. Ahmad, S. Arif, Facile two-step synthesis of yttrium-doped g-C_3N_4 for enhanced photocatalytic degradation of methylene blue with self-cleaning properties, Nanoscale Adv. 8 (2026) 565-579. https://doi.org/10.1039/d5na00600g.

[31] É.W.A. Almeida, C.M.C. Dazon, M.D.V. Rodriguez, et al., Graphitic Carbon Nitride: Synthesis and Characterization, Monolayer at the Air-Water Interface, Langmuir-Blodgett Films, and Its

Photocatalytic Performance, ACS Omega 10 (2025) 17024-17032. https://doi.org/10.1021/acsomega.5c02295.

[32] X. Bi, L.Z. Wang, D.H. Zhai, et al., DuIn-situ synthesis of g-C_3N_4 with nitrogen vacancy and cyano group via one-pot method for enhanced photocatalytic activity, Sci. Rep. 15 (2025) 19864. https://doi.org/10.1038/s41598-025-03286-z.

[33] J.N. Zhu, X.Q. Zhu, F.F. Cheng, et al., Preparing copper doped carbon nitride from melamine templated crystalline copper chloride for Fenton-like catalysis, Appl. Catal. B 256 (2019) 117830. https://doi.org/10.1016/j.apcatb.2019.117830.

[34] B. Dai, X. Chen, X. Yang, et al., Designing S-scheme Au/g-C_3N_4/$BiO_{1.2}I_{0.6}$ plasmonic heterojunction for efficient visible-light photocatalysis, Sep. Purif. Technol. 287 (2022) 120546. https://doi.org/10.1016/j.seppur.2022.120531.

[35] B. Bhargawa, S. Shanmugasundaram, K.P. Kangeyan, et al., Synergistic piezo-photocatalytic degradation of ciprofloxacin by g-C_3N_4/ZnO heterojunction, Sep. Purif. Technol. 389 (2026) 136903. https://doi.org/10.1016/j.seppur.2026.136903.

[36] G. Zhou, F. Yang, X. Zhu, et al., Copper-Copper Oxide Heterostructural Nanocrystals Anchored on g-C_3N_4 Nanosheets for Efficient Visible-Light-Driven Photo-Fenton-like Catalysis, Molecules 30 (2025) 144. https://doi.org/10.3390/molecules30010144.

[37] R. Chen, Q. Wang, G. Gao, et al., Lanthanide-titanium oxo cluster and $BiVO_4$ Z-scheme photocatalyst sheets for carbon dioxide reduction, ACS Catal. 14 (2024) 12234-12241. https://doi.org/10.1021/acscatal.4c03595.

[38] Y. Zhong, S. Chen, T. Xiao, et al., Interfacial modification of $BiVO_4$ photocatalyst: construction of heterojunction with AgI, Phys. Chem. Solids 202 (2025) 112691. https://doi.org/10.1016/j.jpcs.2025.112691.

[39] S. Hou, X. Gao, X. Lv, et al., Decade milestone advancement of defect engineered g-C_3N_4 for solar catalytic applications, Nano Micro Lett. 16 (2024) 70. https://doi.org/10.1007/s40820-023-01297-x.

[40] T. Zhou, H. Wei, B. Xiao, et al., Anchored Cu single atoms on porous g-C3N4 for superior photocatalytic H_2 evolution from water splitting, RSC Adv. 13 (2023) 8915-8922. https://doi.org/10.1039/d3ra00775h.

[41] C.J. Chang, C.T. Li, J.K. Chen, et al., Rod-Like $BiVO_4$-$Bi_2O_2CO_3$ Nanosheet Composites as

Photocatalysts for Hydrogen Generation, ACS Appl. Nano Mater. 8 (2025) 20509-20522. https://doi.org/10.1021/acsanm.5c03782.

[42] N.T. Huyen, T. Luu, T. Le, et al., Structure-property-performance correlation in $BiVO_4$ photoanodes synthesized by intensity-tuned pulse electrodeposition, Nanoscale Adv. 7 (2025) 7182-7195. https://doi.org/10.1039/d5na00667h.

[43] W.T. Chen, H.W. Shiu, Y.X. Chen, et al., Highly Selective Toward HER or CO_2RR by Regulating Cu Single and Dual Atoms on g-C_3N_4, Adv. Funct. Mater. 36 (2026) e14183. https://doi.org/10.1002/adfm.202514183.

[44] Y. Ding, S. Maitra, C.H. Wang, et al., Bi-functional Cu-TiO_2/CuO photocatalyst for large-scale synergistic treatment of waste sewage containing organics and heavy metal ions, Sci. China Mater. 66 (2023) 179-192. https://doi.org/10.1007/s40843-022-2148-4.

[45] T. Tran, P. Le, T. Ngo, et al., An investigation on the visible light-driven Z-scheme $BiVO_4$/g-C_3N_4 heterostructures: Performance, evaluation, and mechanism for dye and antibiotics degradation, Mater. Today Commun. 40 (2024) 109373. https://doi.org/10.1016/j.mtcomm.2024.109373.

[46] M. Xue, Y. Dong, X. Ye, et al., Sulfur Vacancy-Rich ZnS/ZnCdS S-Scheme Heterojunction for Efficient Photocatalytic Hydrogen Evolution Under Visible-Light Irradiation, Adv. Funct. Mater. 36 (2026) e76575. https://doi.org/10.1002/adfm.76575.

[47] X. Zhang, F. Li, Y. Guo, et al., Advances in Photocatalytic Degradation of Volatile Organic Compounds Using Bismuth-Based Catalysts (A Review), Russ. J. Gen. Chem. 96 (2026) 221. https://doi.org/10.1134/S107036322660092X.

[48] B.F. Luo, F. Xia, Y.H. Ran, et al., Sulfur Vacancy-Engineered 2D/2D $ZnIn_2S_4$/Zn-TCPP S-Scheme Heterojunction for Efficient Photocatalytic H_2O_2 Production, Small 22 (2026) e74196. https://doi.org/10.1002/smll.74196.

[49] P.A. Ajibade, F.P. Andrew, T.B. Mbuyazi, et al., Enhanced Photocatalytic Degradation of trypan Blue Dye by Copper Sulfide Nanoparticles Prepared from 4-Benzylpiperazinyldithiocarbamate Copper(II) Complex, ACS Omega 10 (2025) 45090-45102. https://doi.org/10.1021/acsomega.5c03931.

[50] Y. Xie, B. Dong, X. Wang, et al., Construction of core-shell $CoSe_2$/$ZnIn_2S_4$ heterostructures for efficient visible-light-driven photocatalytic hydrogen evolution, Dalton Trans. 53 (2024) 675-683. https://doi.org/10.1039/d3dt03379a.

[51] P. Dhatshanamurthi, M. Shanthi, Enhanced photocatalytic degradation of azo dye in aqueous solutions using Ba@Ag@ZnO nanocomposite for self-sensitized under sunshine irradiation, Int. J. Hydrogen Energy 42 (2017) 5523-5536. https://doi.org/10.1016/J.IJHYDENE.2016.08.089.

[52] F.T. Geldasa, F.B. Dejene, First Principles Investigation of Niobium and Carbon-Doped Titanium Dioxide for Enhanced Visible Light Photocatalytic Activity, Chem. Select. 10 (2025) e04529. https://doi.org/10.1002/slct.202504529.

[53] H.A.E. Omr, Y.T. Wu, Y.H. Siao, et al., $ZnIn_2S_4$/ZnO Film for High-Efficiency CO_2 Conversion to Fuel: Photocatalysis by Atomically Disorder-Engineered Heterointerface, ACS Appl. Mater. Interfaces 17 (2025) 47625-47636. https://doi.org/10.1021/acsami.5c08784.

[54] L. Xu, J. Sun, Y. Zhang, et al., Improved Photocatalytic CO_2 Reduction via Engineering Zinc Vacancies in S-Scheme ZnO/$ZnIn_2S_4$ Heterostructures, ACS Appl. Energy Mater. 8 (2025) 12303-12315. https://doi.org/10.1021/acsaem.5c01803.

[55] K. Su, L. Zheng, M. Liu, et al., Oxygen vacancies regulated S-scheme charge transport route in $BiVO_4$-OVs/g-C_3N_4 heterojunction for enhanced photocatalytic performance, Small 20 (2024) 2405551. https://doi.org/10.1002/smll.202405551.

[56] Q. Wang, Y. Li, F. Huang, S. Song, G. Ai, X. Xin, B. Zhao, Y. Zheng, Z. Zhang, Recent advances in g-C_3N_4-based materials and their application in energy and environmental sustainability, Molecules 28 (2023) 432. https://doi.org/10.3390/molecules28010432.